Structural and Electrochemical Investigation of Zinc-Doped Lithiated MoO₃ Cathode Materials for Lithium-Ion Batteries

Jianyong Wang[1,2], Jiayuan Shi[2,], Bin Shi[2], Yunhuai Zhang[1,*]*

[1] College of Chemistry and Chemical Engineering, Chongqing University, Chongqing 400044, China
[2] State Key Laboratory of Advanced Chemical Power Sources (SKL-ACPS), Guizhou Meiling Power Sources Co., Ltd., Guizhou, 563003, P. R. China
[*]E-mail: jiayshi@163.com (J. Shi), zyh2031@cqu.edu.cn (Y. Zhang)

In this study, the microplates of zinc-doped lithiated MoO₃ cathode materials have been successfully prepared through a facile one-pot method. The XRD, XPS and the ICP results show that the zinc-doping of MoO₃ favors $Li_{0.042}MoO_3$ phase formation in the crystal lattice of the product, which can result in the improvement of the electrical conductivity of the MoO₃ cathode. By comparing with the SEM images of the pristine MoO₃ material, the SEM images show that the zinc-doping and lithiation can reduce the size and thickness of MoO₃ particles. When the zinc-doped lithiated MoO₃ (ZLMO-2) is used as a cathode material for lithium-ion batteries, it delivers an initial discharge capacity of 341.7 mAh·g⁻¹ at a current density of 30 mA·g⁻¹. Moreover, ZLMO-2 shows a cyclic stability (capacity retention of 57.9% after 100 cycles) and rate capability that are better than those of pristine MoO₃. This can be attributed to the increased conductivity and ion diffusivity achieved by MoO₃ lithiation and the enhanced electrochemical stability achieved by the pillar effect of zinc doping.

1. INTRODUCTION

With the explosive development of modern technology, human demand for energy sources and energy storage has significantly increased [1, 2]. As a new kind of energy storage devices, lithium-ion batteries have attracted the extensive attention of society because of their relatively high energy density and long cycle life [3-5]. For instance, olivine-type LiFePO₄, an attractive cathode material with a relatively high discharge voltage (3.4 V), good cycling stability, favorable thermal stability and low material cost, has been widely applied to lithium-ion batteries in medical planted instruments and movable power sources [6]. However, LiFePO₄ shows some fundamental defects, e.g., intrinsic poor conductivity and limited theoretical specific capacity (*ca.* 170 mAh·g⁻¹), which restrict its application in

high-power battery materials [7]. Therefore, the exploration of novel cathode materials with a higher capacity and energy density is momentous for improving the electrochemical performance of lithium-ion batteries [8].

Molybdenum possesses multiple valence states, and its compounds can exhibit rich chemical properties [9]. Many researchers have paid attention to Mo-based oxides, dichalcogenides and oxysalts containing MoO_2, MoO_3, MoO_{3-y} ($0 \leq y \leq 1$), MMo_xO_y (M = Fe, Co, Ni, Ca, Mn, Zn, Mg or Cd; x = 1, y = 4; x = 3, and y = 8), MoS_2, $MoSe_2$, $(MoO_2)_2P_2O_7$, $LiMoO_2$ and Li_2MoO_3 as promising candidates for electrochemical energy storage systems [10, 11]. As a layered n-type semiconductor, MoO_3 has been put into practice as catalysts, gas sensors, batteries, lubricants, memory materials and electrochromic devices [12, 13]. MoO_3 is a crucial transition metal oxide with a high theoretical specific capacity (372 mAh·g^{-1}) and energy density (930 Wh·kg^{-1}) and is an alluring cathode material for lithium-ion batteries [14]. Due to the different arrangements of MoO_6 octahedrons in the crystal structures, molybdenum trioxide mainly exists in three phase structures, one of which is the thermodynamically stable orthorhombic phase (α type) MoO_3, and the other two are metastable structures, including the monoclinic phase (β type) and hexagonal phase (h type) [15]. For α-MoO_3, the tetrahedral and octahedral cavities in its structure are suitable for the intercalation and deintercalation of lithium ions [16, 17]. For h-MoO_3, its basic building unit is a distorted MoO_6 octahedron, in which the structural elements form a chain with a common ridge, and the hexagonal phase MoO_3 structure is formed by the three-dimensional accumulation of the chains. The h-MoO_3 structure contains an empty near-hexagonal channel, and this special structure with a three-dimensional network is favorable for lithium ions to move in the crystal cavity [18]. The monoclinic phase β-MoO_3, composed of common-shaded octahedrons, is a twisted three-dimensional ReO_3-type structure [19]. Based on the abovementioned structural study, MoO_3 is considered to be a promising candidate for next-generation secondary lithium battery electrode materials due to its unique stable layered structure and its ability to generate oxygen vacancies [20]. However, the theoretical capacity of MoO_3 cannot be easily reached, and its discharge capacity is difficult to maintain upon repeated electrochemical cycles due to its poor ionic and electronic conductivity [21]. Moreover, the irreversible intercalation of lithium ions is inevitable during charging-discharging cycles, which becomes the hindrance to improving the performance of MoO_3 [22]. Therefore, many methods have been reported for improving the electrochemical performance of MoO_3, such as conducting coatings [23], structural modification and hybrid doping [24, 25]. In addition, size control and nanocrystallization have also become effective methods of improving the electrochemical performance of MoO_3 [26].

The Zn-doping of electrode materials has been utilized in the literature to improve the performance of lithium-ion batteries. For example, Liu et al. prepared $LiZn_{0.01}Fe_{0.99}PO_4$ to increase the lattice volume of a $LiFePO_4$ crystal without destroying its lattice structure [27]. the doped zinc atoms can protect the $LiFePO_4$ crystal from volume change and structure collapse during electrochemical cycling. The pillar effect of zinc atoms provides more room for lithium ion motion, thereby lowering the charge transfer resistance and accelerating lithium ion diffusion. Guangda Li et al. fabricated hollow Zn-doped Fe_2O_3 nanospheres for use as anode materials in lithium-ion batteries [28]. The partial replacement of Fe with Zn in the crystal structure of Fe_2O_3 can cause an increase in the unit cell volume, because the radius of Zn^{2+} (0.074 nm) is larger than that of Fe^{3+} (0.055 nm). The larger cell volume makes lithium ion diffusion easier. Therefore, Zn doping plays an important role in the stability of the crystal lattice.

Valanarasu et al. reported the suppression of Co^{4+} dissolution in $LiCoO_2$ through the formation of a solid solution between cobalt and Zn ions, leading to the improvement in the capacity retention of a commercial $LiCoO_2$ cathode by Zn doping [29]. Moreover, the conductivity of cathode materials such as $LiFePO_4$ can be effectively enhanced and their rate capability can be improved through zinc doping [30-34]. Recently, Zn-doped molybdenum-based compounds have been studied in the field of semiconductor devices and electronic and optoelectronic applications. Zn doping has been proved to be an effective method for adjusting the crystal structure and modulating the band gap of molybdenum-based compounds (e.g., MoO_3 and MoS_2). For example, the crystal growth of the MoO_3 structure can be limited, and the oxygen vacancies in the lattice can be increased due to the ionic radius difference between Zn^{2+} and Mo^{6+} [35-37]. However, to the best of our knowledge, few reports have been presented on the electrochemical performance of Zn-doped lithiated MoO_3 cathode materials for lithium-ion batteries.

2. EXPERIMENTAL

2.1. Synthetic procedures

In a typical procedure, lithium acetate ($CH_3COOLi \cdot 2H_2O$, 18 mmol, 1.834 g) was first mixed in 5 mL of concentrated hydrochloric acid (HCl, 36 wt%), and the resultant solution was labeled Solution A. An appropriate amount of $(CH_3COO)_2Zn \cdot 2H_2O$ was dissolved in 10 mL of acetonitrile, and the resulting solution was named Solution B. Then, 8 mmol (0.768 g) of molybdenum powder was dissolved in 5 mL of hydrogen peroxide (H_2O_2, 30 wt%) to obtain a yellow solution, which was named Solution C. The abovementioned Solutions A and B were added into Solution C and stirred at room temperature for 30 minutes. The resulting mixture was then transferred into a Teflon lined autoclave, and the reaction temperature was kept at 180 °C for 24 h. After the autoclave was cooled to room temperature, the precipitate was filtered out and rinsed three times with deionized water and ethanol. Then, the obtained powder was dried at room temperature for 6 h and calcined at 600 °C for 10 h in air. The samples were named LMO, ZLMO-1, ZLMO-2 and ZLMO-3 when the reactant mole ratios of Zn/Mo/Li were 0:8:18, 0.5:8:18, 1:8:18 and 2:8:18 in the synthesis systems, respectively. For comparison, the pristine molybdenum trioxide structures were named MoO_3 and prepared by using analogous procedures without the addition of $CH_3COOLi \cdot 2H_2O$ or $(CH_3COO)_2Zn \cdot 2H_2O$. The Zn-doped MoO_3 material named ZMO was also obtained using a method similar to the method used to prepare Sample ZLMO-2, except for the addition of $CH_3COOLi \cdot 2H_2O$.

2.2. Materials Characterization

X-ray diffraction (XRD, ARL EQUINOX 3000, America) measurements were performed by a powder X-ray diffractometer with a Cu Kα source having a wavelength of 1.5406 Å to investigate the crystallographic information, and data were collected in the scanning range of 5°-70° at a scan rate of 60°/min. Scanning electron microscopy (SEM) images were obtained using a field-emission scanning

electron microscope (FEI Quanta 250, America) to observe the surface morphology and particle size. The high resolution transmission electron microscopy (HRTEM) image and selected area electron diffraction (SAED) pattern were taken with a JEOL JEM-2010 microscope (Japan) at an acceleration voltage of 20 kV. The as-prepared samples were dissolved in ethanol, and drops of the solution were placed on a film of a carbon-supported copper grid. Then, the X-ray photoelectron spectroscopy (XPS) analysis was performed by an ESCALAB 250Xi spectrometer (Thermo Fisher Scientific, America) equipped with an Al Kα (1486.6 eV) X-ray source. Inductively coupled plasma optical emission spectroscopy (ICP-OES) (AGILENT ICPOES730, America) was employed to determine the mass ratio of Li, Zn and Mo in the final products.

2.3. Electrochemical test

The electrochemical properties of the samples were measured by assembling 2032 coin-type cells. The working electrode was prepared by mixing 80 wt% active materials with 10 wt% super P and 10 wt% polyvinylidene fluoride (PVDF) in an appropriate amount of N-methyl-2-pyrrolidine with an ultrasonication-assisted treatment. The slurry of the uniform mixture was spread on aluminum current collectors and dried at 120 °C for 12 h in a vacuum oven. The loading mass of the active material on the current collector is 2–3 mg. Using Li foil as the anode electrode, the as-prepared cathode films were assembled into coin-type cells in an argon filled glove box, Celgard 2400 was used as the separator, and 1 M $LiPF_6$ in a mixture of ethylene carbonate (EC) and dimethyl carbonate (DEC) (1:1, v/v) was used as the electrolyte. The cells were cycled galvanostatically at various currents (0.03 $A \cdot g^{-1}$, 0.05 $A \cdot g^{-1}$, 0.1 $A \cdot g^{-1}$, 0.2 $A \cdot g^{-1}$, 0.5 $A \cdot g^{-1}$ and 1 $A \cdot g^{-1}$) in a voltage range of 1.5-4.5 V (vs. Li/Li^+) at 25 °C. Electrochemical impedance spectroscopy (EIS) was performed using a VersaSTAT 3F electrochemical workstation over the frequency range from 10 mHz to 100 kHz and with an amplitude of 5 mV. In addition to using the abovementioned equipment, the cyclic-voltammetry (CV) measurements can be recorded at a scanning rate of 0.2 $mA \cdot s^{-1}$ in the potential window of 1.5 to 4.2 V (vs. Li^+/Li).

3. RESULTS AND DISCUSSION

XRD measurements are employed to investigate the phase composition and crystal structure of the synthesized samples with different chemical compositions (MoO_3, LMO, ZMO and ZLMOs). Fig. 1 shows their resultant diffraction patterns and the standard XRD patterns of MoO_3, $Li_{0.042}MoO_3$ and ZnO as references. For pristine MoO_3, all of its peaks can be indexed to the orthorhombic phase of MoO_3 belonging to the space group Pnma(62) (JCPDS card No. 65-2421). The three strongest peaks at $2\theta =$ 23.4°, 25.8° and 27.3° can be ascribed to the (110), (040) and (021) planes of the orthorhombic MoO_3 phase, respectively. No unpredictable peaks of other phases can be detected, indicating the single-phase structure of MoO_3 without any impurities. Zinc-doped MoO_3 (ZMO) shows similar results to those of pristine MoO_3, and no peaks corresponding to ZnO can be found. This demonstrates that the zinc element is not presented as a separate phase in the product, which is due to the acidic environment of crystal

growth, inhibiting ZnO deposition. Similarly, it is reasonable to observe that no ZnO phase was present in the XRD pattern of the zinc-doped lithiated MoO_3 samples, including ZLMO-1, ZLMO-2 and ZLMO-3. Compared with the XRD pattern of the lithium-free samples (MoO_3 and ZMO), the lithiated MoO_3 samples, including LMO, ZLMO-1, ZLMO-2 and ZLMO-3, show simultaneous strengthening peaks at 12.7°, 25.8° and 38.8° corresponding to the (020), (040) and (060) planes of the orthorhombic $Li_{0.042}MoO_3$ phase [38]. To study the phase composition of the products, the area ratios of the four peaks at 12.7°, 23.4°, 25.8° and 38.8° have been calculated, while the areas of the peaks at 23.4 ° are denoted as 1.00 in all six products. The results are listed in Table 1. ZMO shows similar relative intensities to those of MoO_3, while the relative intensities of the peaks at 12.7°, 25.8° and 38.8° simultaneous increase in the order of MoO_3 < LMO < ZLMO-1 < ZLMO-2 < ZLMO-3. Therefore, the lithiation of MoO_3 can lead to the formation of the $Li_{0.042}MoO_3$ phase in the LMO sample, and the zinc-doping of the lithiated MoO_3 samples may favor more lithium ions entering the crystal lattice of lithiated MoO_3, thus increasing the lithiation degree of the products. This may be due to the pillar effect of zinc-doping, which can provide more space for Li-ion intercalation [29, 34, 39].

Table 1. The relative intensities of the peaks at 12.7°, 25.8° and 38.8° relative to the peaks at 23.4° in all six products (intensity of the peaks at 23.4° is counted as 1.00).

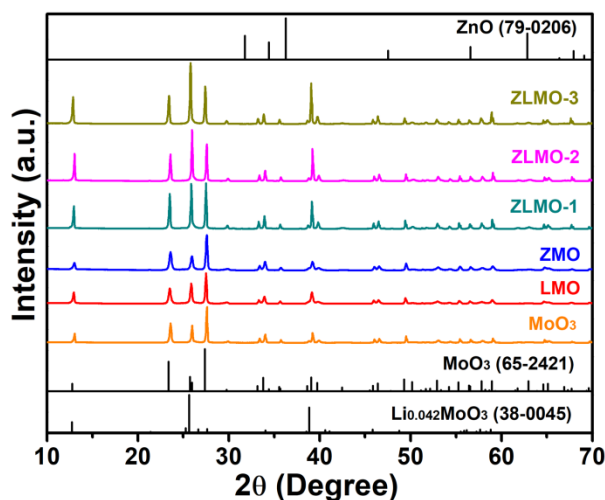| 2θ	12.7	23.4	25.8	38.8
MoO_3	0.36	1.00	0.75	0.38
ZMO	0.32	1.00	0.76	0.37
LMO	0.51	1.00	1.08	0.52
ZLMO-1	0.56	1.00	1.28	0.56
ZLMO-2	0.81	1.00	1.74	0.87
ZLMO-3	0.85	1.00	1.96	1.03

Figure 1. XRD patterns of pristine MoO_3, ZMO, LMO, ZLMO-1, ZLMO-2 and ZLMO-3, which were obtained using standard patterns of MoO_3 and $Li_{0.042}MoO_3$ as the references.
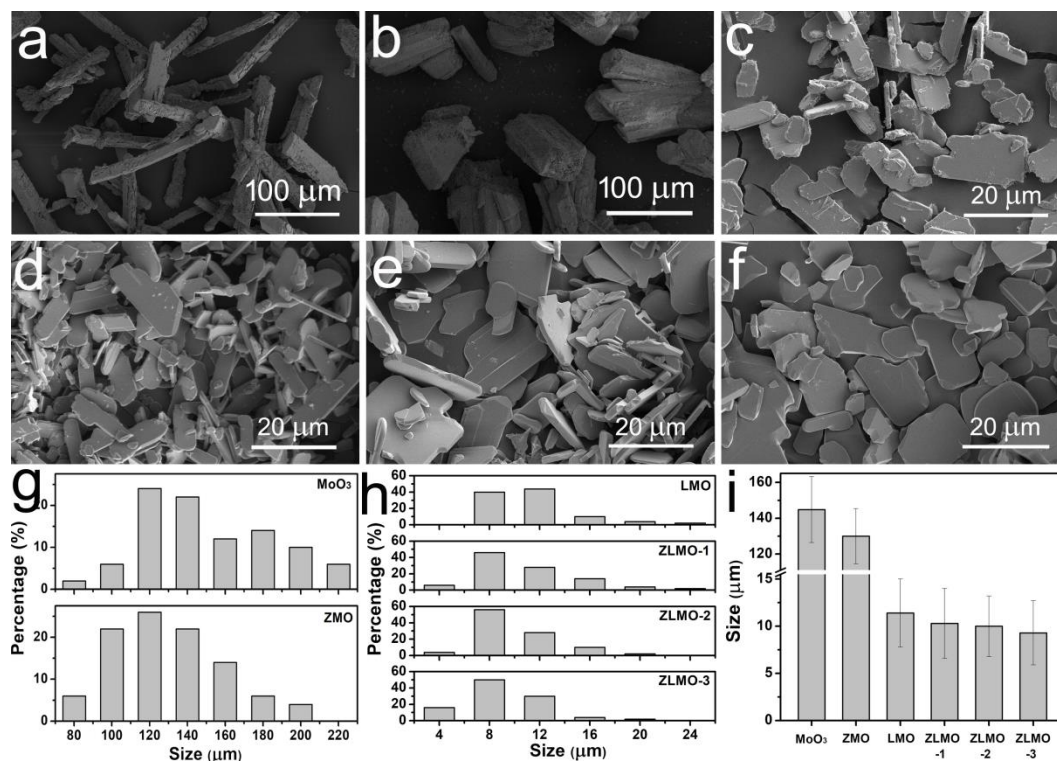
Figure 2. FE-SEM images of (a) MoO₃, (b) ZMO, (c) LMO, (d) ZLMO-1, (e) ZLMO-2 and (f) ZLMO-3; size distribution of (g) MoO₃ and ZMO, (h) LMO, ZLMO-1, ZLMO-2 and ZLMO-3; and (i) average sizes of all six samples.

The particle size and crystal morphology of MoO₃, LMO, ZMO and ZLMOs are examined by using FE-SEM, as shown in Fig. 2a-f. Moreover, the particle size distribution of each sample is statistically analyzed by measuring 100 particles from the SEM images obtained for each sample, and the corresponding results are shown in Fig. 2g-h. Finally, the average size of these samples (Fig. 2i) is calculated based on the above-mentioned statistical results by using the following equation (1):

$$d_{\text{SEM}} = \frac{\sum n_i \cdot d_i}{\sum n_i} \quad (1)$$

where d_i and n_i represented the particle size and the number of particles with the diameter of d_i, respectively. Compared with the columnar structures of the lithium-free samples (MoO₃ and ZMO) with sizes ranging from 80 to 220 μm, the lithiated samples, including LMO and ZLMOs, show plate morphology with smaller sizes (4-24 μm) and reduced thicknesses. Therefore, lithiation has a significant effect on particle size, while zinc-doping has a much less significant influence than lithiation on the size and morphology of the products. Concretely speaking, the sizes of the lithiated samples are one order of magnitude smaller than those of the lithium-free samples, while the zinc-doped MoO₃ and zinc-doped lithiated MoO₃ samples are slightly smaller than the MoO₃ and lithiated MoO₃ samples, respectively. The average particle size decreases in the order of MoO₃ (144.8μm) > LMO (130.0 μm) > ZMO (11.4 μm) > ZLMO-1 (10.3 μm) > ZLMO-2 (10.0 μm) > ZLMO-3 (9.3 μm) (Fig. 2i).

To further investigate the crystal structure of the zinc-doped lithiated MoO₃ (ZLMO-2) sample, an HRTEM image and a selected area electron diffraction (SAED) pattern are obtained, as shown in Fig.

3a and 3b. The HRTEM image obtained from the edge of the belts of ZLMO-2 shows clear lattice fringes. The interplanar spacings of 0.198 nm, 0.185 nm and 0.136 nm are assigned to the (200), (002) and (202) lattice planes of orthorhombic MoO_3, respectively. The sharp diffraction spots in the SAED pattern also indicate the high crystallinity of ZLMO-2 with a large (010) crystal plane.
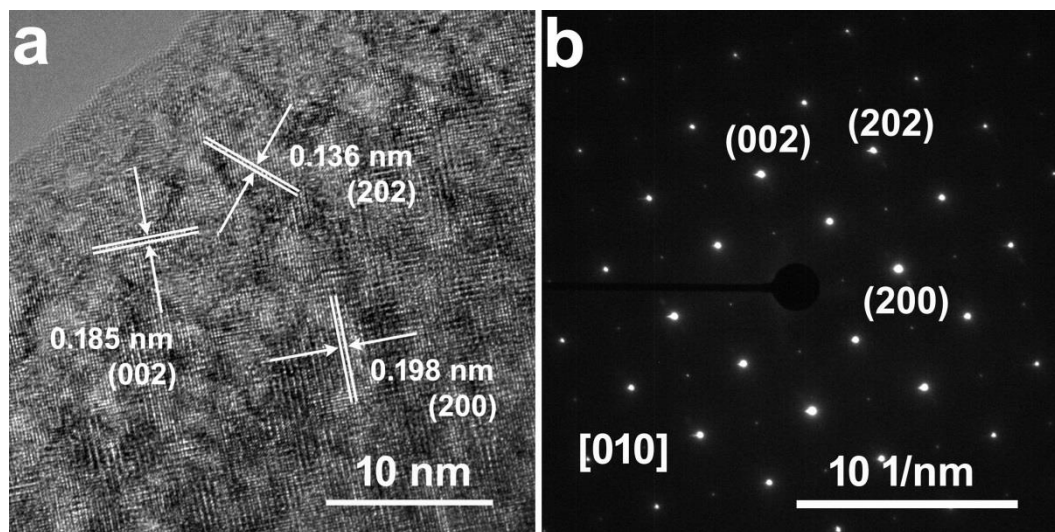

Figure 3. (a) HRTEM image and (b) SAED pattern of ZLMO-2.

The chemical composition and valence states of ZLMO-2 were measured by XPS, as presented in Fig. 4. The full spectra in the energy range of 25–1100 eV shows peaks at approximately 55.6, 284.8, 531.9, 1021.7 and 233.0 eV, which correspond to Li_{1s}, C_{1s}, O_{1s}, Zn_{2p} and Mo_{3d}, respectively (Fig. 4a), indicating the presence of lithium, carbon, oxygen, zinc and molybdenum elements in the sample. Fig. 4b shows the Zn $2p_{3/2}$ and Zn $2p_{1/2}$ spectrum at 1021.7 eV and 1044.2 eV, which is consistent with the oxidation state of Zn^{2+} in the sample [28, 40]. As shown in Fig. 4c, the typical two-peak structure of Mo $3d_{5/2}$ at 232.8 eV and Mo $3d_{3/2}$ at 236.0 eV was observed, and the binding energy position agrees well with that appearing in MoO_3 [41], suggesting that the oxidation state of Mo in ZLMO-2 is +6. The samples' Li/Mo and Zn/Mo molar ratios are detected by ICP, as shown in Table 2. The result demonstrates that both the Li/Mo and Zn/Mo ratios increase in the order of LMO < ZLMO-1 < ZLMO-2 < ZLMO-3, indicating that zinc addition is beneficial to lithium ions entering the crystal lattice of the cathode materials [42]. Therefore, the ICP results agree with those obtained from the XRD measurements.
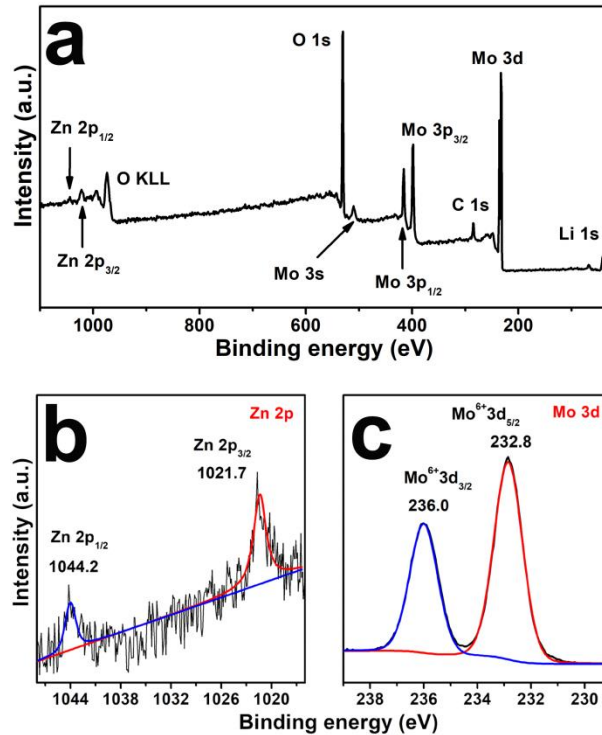
Figure 4. XPS spectra of ZLMO-2, including the (a) survey spectra, (b) Zn 2p spectra and (c) Mo 3d spectra.

Table 2. The molar ratio of Zn/Mo and Li/Mo, the calculated molar percentage of $Li_{0.042}MoO_3$ [n($Li_{0.042}MoO_3$)/n(Mo)] and kinetic parameters of pristine MoO_3, ZMO, LMO, ZLMO-1, ZLMO-2 and ZLMO-3.

Sample	MoO_3	ZMO	LMO	ZLMO-1	ZLMO-2	ZLMO-3
n(Zn)/n(Mo)	0	$4.47*10^{-3}$	0	$2.90*10^{-3}$	$4.14*10^{-3}$	$6.07*10^{-3}$
n(Li)/n(Mo)	0	0	$2.12*10^{-3}$	$2.79*10^{-3}$	$3.09*10^{-3}$	$4.32*10^{-3}$
n($Li_{0.042}MoO_3$)/n(Mo)	0	0	5.05%	6.64%	7.36%	10.3%
R_s (Ω)	7.20	4.85	4.48	3.49	3.33	3.42
R_{sl} (Ω)	107	104	99.2	36.2	29.0	39.1
R_{ct} (Ω)	232	195	182	133	63.4	70.3
D ($cm^2 \cdot s^{-1}$)	$2.7*10^{-15}$	$1.0*10^{-14}$	$1.6*10^{-14}$	$1.8*10^{-14}$	$1.4*10^{-13}$	$6.3*10^{-14}$

　　　To further understand the resistances and diffusion behavior of the six samples, EIS has been conducted. Fig. 5a displays the typical Nyquist plots, and the inset of Fig. 5a is the equivalent circuit, which is used to fit the spectra. All the EIS curves consist of a depressed semicircle at high and medium frequency regions as well as an inclined line at the low frequency region [43]. The R_s, R_{sl}, R_{ct}, C_{sl}, C_{ct} and Z_w variables in the equivalent circuit represent the electrolyte resistance, the surface layer resistance, the charge-transfer resistance, the surface layer capacitance, the double layer capacitance, and the Warburg diffusion impedance, respectively. The values of $R_{sl}+R_{ct}$ are approximately 339, 281 and 92 Ω for MoO_3, LMO and ZLMO-2, respectively, as listed in Table 2. Thus, the lithiation process endows the

MoO_3 cathode material with a better electronic conductivity and faster charge transfer than the pristine MoO_3 material, enhancing electron transport and promoting the electrochemical reaction of the cathode materials [9]. Moreover, the zinc-doped lithiated MoO_3 sample (ZLMO-2) has a much lower charge transfer resistance than LMO and MoO_3, which may lead to the higher reversible capacities and better rate performance of the cathode materials. This is because of the pillar effect of zinc atoms, which is beneficial to the formation of the lithiated MoO_3 phase during the synthetic process and favors lithium ion transport during the electrochemical reaction. In addition, the lithium ion diffusion coefficient (D_{Li+}) can be calculated using Equations (2) and (3), as follows:

$$D_{Li+} = R^2T^2/2A^2n^4F^4C\sigma^2 \quad (2)$$

$$Z_{re} = R_s + R_{ct} + \sigma\omega^{-1/2} \quad (3)$$

where R is the gas constant, T is the absolute temperature, A is the electrode area, n is the number of electrons per molecule during oxidation, F is the Faraday constant, C is the concentration of lithium ions, and σ is the Warburg factor, which can be calculated from the slope of the real axis resistance (Z_{re}) vs. the inverse square root of the angular frequency ($\omega^{-1/2}$) according to Fig. 5b and Equation (3). As listed in Table 2, the calculated diffusion coefficient of the samples tends to decline in the order of MoO_3 < ZMO < LMO < ZLMO-1 < ZLMO-3 < ZLMO-2. Therefore, lithium ion diffusion can be facilitated through the lithiation and zinc-doping of MoO_3, thus resulting in the improvement of the electrochemical kinetics.
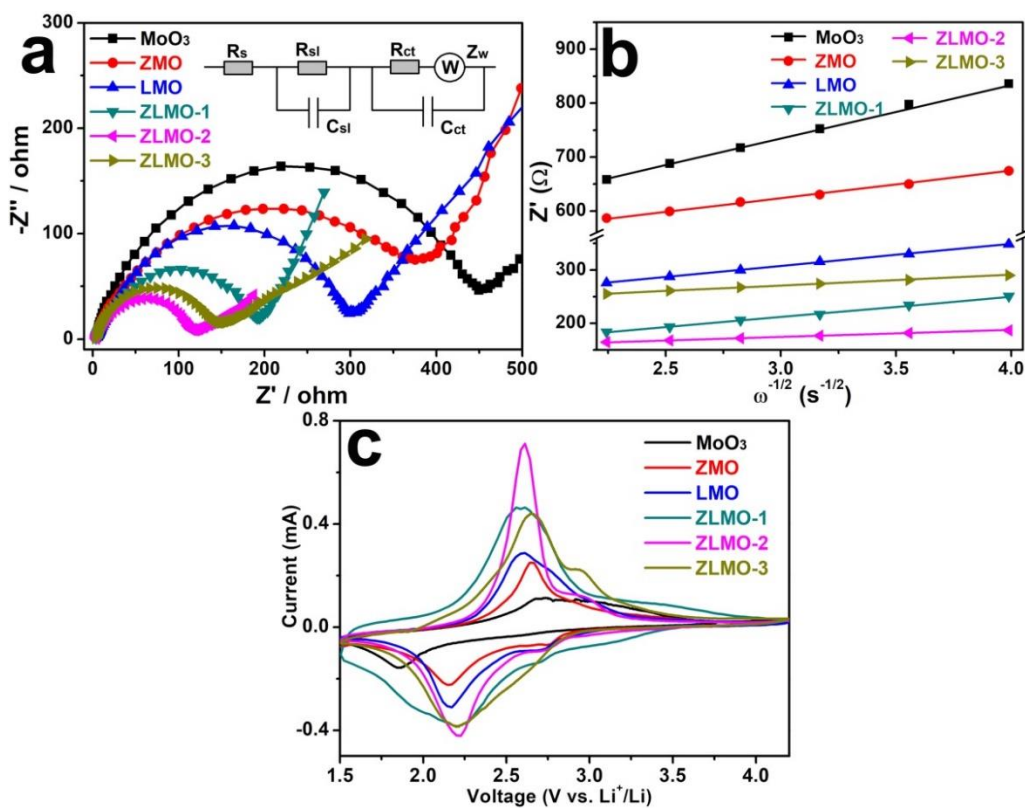

Figure 5. (a) Electrochemical impedance spectra, (b) the relationship between Z' and $\omega^{-1/2}$ at low frequencies and (c) CV curves of pristine MoO_3, ZMO, LMO, ZLMO-1, ZLMO-2 and ZLMO-3.

The cyclic voltammogram profiles of the six samples have been obtained at a scan rate of 0.2 $mV \cdot s^{-1}$ in the potential range of 1.5–4.2 V to show the characteristics of the redox reaction in Li-ion cells with different electrodes. All the spectra exhibit similar shapes (Fig. 5c). Two couples of redox current peaks can be found on each voltammogram curve, corresponding to the insertion/extraction of lithium ions between the MoO_6 octahedron interlayers [21]. No other peaks can be observed, indicating the electrochemical inactivity of zinc within the measured voltage range [44]. For ZLMO-2, the redox current peaks at 2.61 and 2.22 V are stronger than those at 2.99 and 2.73 V, and the potential separation between the two stronger redox current peaks (ΔE) is 0.39 V. Similarly, the ΔE values of the other samples can be calculated as 0.88, 0.50, 0.44, 0.41 and 0.43 V for MoO_3, ZMO, LMO, ZLMO-1 and ZLMO-3, respectively. Compared with the other samples, the narrowest peak separation of ZLMO-2 indicates the reduction of the electrode polarization and the enhancement of the reversibility in the electrode reaction [45]. Moreover, the higher peak currents and larger spectra areas of the lithiated and zinc-doped samples facilitates the improved redox activity and faster reaction kinetics during the insertion and extraction process of lithium ions, which is indicative of the improvement of the electrochemical performance [46]. The area of each cycle (A_i, while i is the cycle times) curve can be calculated through integration, and the cycle efficiency (Q_i) of the ith curve can be obtained by using the following equation (4):

$$Q_i = A_i / A_1 \quad (4)$$

Herein, A_1 is the area of the first cycle curve. The cycle efficiency of the different samples in the initial ten cycles is listed in Table 3. The tenth cycle efficiency (Q_{10}) of pure MoO_3, ZMO, LMO, and ZLMO-2 are 16.3%, 64.6%, 87.8% and 99.7%, respectively. The highest cycle efficiency of ZLMO-2 shows that the enhancement of the cycle stability is realized through the lithiation and zinc-doping of the MoO_3 structures [47].

Table 3. The cycle efficiency of the obtained materials upon different CV cycles.

Sample	Q_2%	Q_3%	Q_4%	Q_5%	Q_6%	Q_7%	Q_8%	Q_9%	Q_{10}%
MoO_3	58.8	38.4	29.7	23.7	23.2	23.0	20.7	17.3	16.3
ZMO	96.3	91.6	86.3	81.2	76.4	72.6	69.5	66.9	64.6
LMO	96.4	95.9	94.4	93.4	92.8	91.2	88.0	87.4	87.8
ZLMO-1	97.5	96.8	96.6	96.2	94.9	94.5	93.8	93.6	92.3
ZLMO-2	99.6	100.3	100.2	99.7	99.8	99.9	99.3	99.6	99.7
ZLMO-3	101.0	101.2	100.1	99.6	99.9	99.7	99.2	99.1	98.4

To show the advantages of lithiation and zinc doping for MoO_3 cathode materials, the cycling behavior of three zinc-doped lithiated MoO_3 samples was investigated between 1.5 V and 4.5 V at 30 $mA \cdot g^{-1}$. For comparison, the bare MoO_3, lithiated MoO_3 and zinc-doped MoO_3 samples were also tested under the same conditions (Fig. 6a). The specific discharge capacity of the pristine MoO_3 sample decreased to 20 $mAh \cdot g^{-1}$ after 10 cycles, indicating its rapid capacity fade during cycling. Comparatively speaking, the capacity retentions of the zinc-doped MoO_3 (ZMO) and lithiated MoO_3 (LMO) samples after 100 cycles are 23.8% and 36.3%, respectively, showing a better electrochemical stability than

pristine MoO_3. Moreover, the three zinc-doped lithiated MoO_3 samples, including ZLMO-1, ZLMO-2 and ZLMO-3, show higher discharge capacities (141.4, 217.8 and 195.0 mAh·g^{-1}) and capacity retentions (39.0%, 57.9% and 52.5%) than the other samples after 100 cycles, indicating their better cycle performance. Compared with other reported lithiated MoO_x samples, the Zn-doped lithiated MoO_3 sample in this work showed a superior cycling performance (Table 4). The rate performances of the samples were compared at different current rates from 0.03 A·g^{-1} to 1 A·g^{-1} at room temperature. Obviously, the discharge capacity of the samples decreased as the current density increased, which is due to increasing the polarization [48]. The rate performance of ZLMO-2 is the best among all the samples (Fig. 6b). The average specific capacities of ZLMO-2 are 243.5, 194.6, 157.2, 112.2 and 74.0 mAh·g^{-1} at 0.05, 0.1, 0.2, 0.5 and 1 A·g^{-1}, which are equivalent to 74.3%, 59.4%, 48.0%, 34.2% and 22.6% of the capacity obtained at 0.03 A·g^{-1}. The electrochemical improvement is mainly due to the increased conductivity and ion diffusivity achieved by lithiation and the enhanced electrochemical stability achieved by zinc doping, as indicated by the EIS and CV results of the samples.
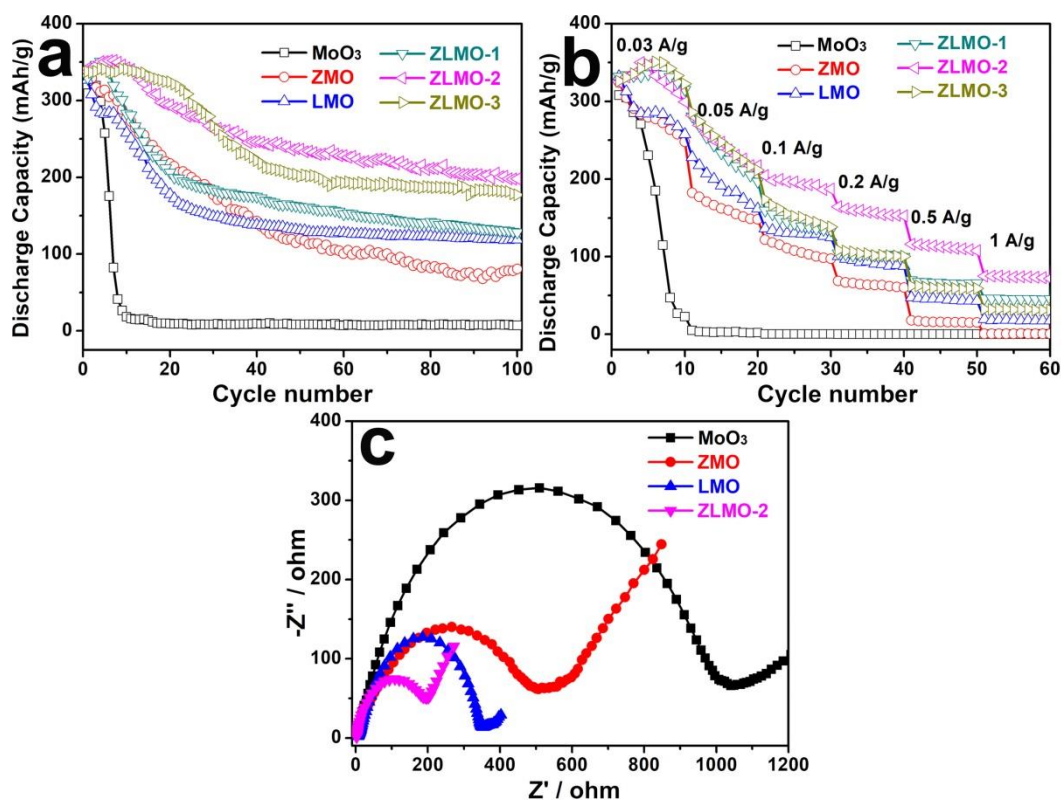

Figure 6. (a) The cycling performance at the current density of 0.03 A·g^{-1} and (b) the rate performance of pristine MoO_3, ZMO, LMO, ZLMO-1, ZLMO-2 and ZLMO-3; (c) the electrochemical impedance spectra of MoO_3, ZMO, LMO and ZLMO-2 after 100 electrochemical cycles.

Fig. 6c shows the EIS plots of the MoO_3, LMO, ZMO and ZLMO-2 electrodes after 100 cycles. All the curves have been fitted by the given circuit (inserted in Fig. 5a). The $R_{sl}+R_{ct}$ value of MoO_3 is 852 Ω after 100 cycles, which is substantial higher than that at its initial state (339 Ω). However, the

LMO and ZMO electrodes displays lower $R_{sl}+R_{ct}$ values (413 and 263 Ω) after 100 cycles, indicating their improved interfacial and electrochemical stability after lithiation and zinc-doping. Particularly, the ZLMO-2 electrode shows the slowest increase in the $R_{sl}+R_{ct}$ value from 92.4 Ω to 139 Ω after electrochemical cycles, indicating the successful suppression of the impedance rise in the ZLMO-2 electrode. This may be due to the improvement of the ionic conductivity and electronic transmission after the lithiation and zinc-doping of MoO_3, which can effectively suppress the side reaction during electrochemical cycling and result in a better electrochemical performance.

Table 4. Electrochemical property comparison of the reported lithiated MoO_x samples.

Sample	Cycling performance Capacity retention (current density, cycle number)	Ref.
Li_2MoO_3/C	79.5% (16 mA·g^{-1}, 35 cycles)	[49]
Li_2MoO_3	45% (10 mA·g^{-1}, 20 cycles)	[50]
$Li_{1.9}K_{0.1}MoO_3$	56% (16 mA·g^{-1}, 100 cycles)	[51]
Li_xMoO_3	57.1% (30 mA·g^{-1}, 50 cycles)	[52]
Zn-doped Li_xMoO_3	57.9% (30 mA·g^{-1}, 100 cycles)	This work

4. CONCLUSIONS

In summary, the MoO_3 cathode material has been successfully lithiated and zinc-doped through a simple hydrothermal reaction process. The phase analysis performed by XRD, HRTEM and SEAD measurements and the microstructure study performed by SEM observations indicates that the lithiation of MoO_3 can reduce the size and thickness of particles and that zinc-doping can increase the lithiation degree of the products. As shown in the EIS and CV results, the electronic conductivity and lithium ion diffusion can be facilitated through the lithiation and zinc-doping of MoO_3 in the ZLMO-2 sample, thus resulting in the improvement of the electrochemical kinetics. When ZLMO-2 was used as the cathode material for lithium-ion batteries, a 57.9% capacity retention was maintained after 100 charging/discharging cycles. Compared with the pristine MoO_3 material, the enhanced electrochemical performance of ZLMO-2 can be attributed to the reduction in the particle size, and the improvement of the electrical and ionic conductivity and the enhancement of the electrochemical stability were achieved through the lithiation and zinc-doping of MoO_3. Therefore, this work shows zinc-doped lithiated MoO_3 as a novel potential candidate for cathode materials.

References

1. B. Dunn, H. Kamath, J.M. Tarascon, *Science*, 334 (2011) 928.
2. M. Armand, J.M. Tarascon, *Nature*, 451 (2008) 652.

3. B. Scrosati, J. Garche, *J. Power Sources*, 195 (2010) 2419.
4. D. Larcher, J.M. Tarascon, *Nature Chem.*, 7 (2015) 19.
5. P.G. Bruce, S.A. Freunberger, L.J. Hardwick, J.-M. Tarascon, *Nature Mater.*, 11 (2012) 19.
6. C. Masquelier, L. Croguennec, *Chem. Rev.*, 113 (2013) 6552.
7. J. Wang, X. Sun, *Energy Environ. Sci.*, 8 (2015) 1110.
8. J.W. Fergus, *J. Power Sources*, 195 (2010) 939.
9. X. Hu, W. Zhang, X. Liu, Y. Mei, Y. Huang, *Chem. Soc. Rev.*, 44 (2015) 2376.
10. W. Kaveevivitchai, A.J. Jacobson, *Chem. Mater.*, 25 (2013) 2708.
11. V. Aravindan, J. Gnanaraj, Y.-S. Lee, S. Madhavi, *Chem. Rev.*, 114 (2014) 11619.
12. A.M. Hashem, H. Groult, A. Mauger, K. Zaghib, C.M. Julien, *J. Power Sources*, 219 (2012) 126.
13. Y. Dong, S. Li, H. Xu, M. Yan, X. Xu, X. Tian, Q. Liu, L. Mai, *Phys. Chem. Chem. Phys.*, 15 (2013) 17165.
14. H.B. Wu, J.S. Chen, H.H. Hng, X.W. Lou, *Nanoscale*, 4 (2012) 2526.
15. Y. Xu, L. Xie, Y. Zhang, X. Cao, *Electron. Mater. Lett.*, 9 (2013) 693.
16. U.K. Sen, S. Mitra, *RSC Adv.*, 2 (2012) 11123.
17. R. Nadimicherla, W. Chen, X. Guo, *Mater. Res. Bull.*, 66 (2015) 140.
18. J.M. Song, X. Wang, X.M. Ni, H.G. Zheng, Z.D. Zhang, M.R. Ji, T. Shen, X.W. Wang, *Mater. Res. Bull.*, 40 (2005) 1751.
19. D. Mariotti, H. Lindstroem, A.C. Bose, K. Ostrikov, *Nanotechnology*, 19 (2008).
20. M.A. Ibrahem, F.-Y. Wu, D.A. Mengistie, C.-S. Chang, L.-J. Li, C.W. Chu, *Nanoscale*, 6 (2014) 5484.
21. R. Nadimicherla, Y. Liu, K. Chen, W. Chen, *Solid State Sci.*, 34 (2014) 43.
22. S. Li, C.-H. Han, L.-Q. Mai, J.-H. Han, X. Xu, Y.-Q. Zhu, *Int. J. Electrochem. Sci.*, 6 (2011) 4504.
23. F. Leroux, L.F. Nazar, *Solid State Ionics*, 133 (2000) 37.
24. X.-J. Wang, R. Nesper, C. Villevieille, P. Novak, *Adv. Energy Mater.*, 3 (2013) 606.
25. S.-H. Lee, R. Deshpande, D. Benhammou, P.A. Parilla, A.H. Mahan, A.C. Dillon, *Thin Solid Films*, 517 (2009) 3591.
26. X.-Y. Xue, Z.-H. Chen, L.-L. Xing, S. Yuan, Y.-J. Chen, *Chem. Commun.*, 47 (2011) 5205.
27. H. Liu, Q. Cao, L.J. Fu, C. Li, Y.P. Wu, H.Q. Wu, *Electrochem. Commun.*, 8 (2006) 1553.
28. G. Li, X. Xu, R. Han, J. Ma, *CrystEngComm*, 18 (2016) 2949.
29. S. Valanarasu, R. Chandramohan, J. Thirumalai, T.A. Vijayan, *Ionics*, 18 (2012) 39.
30. A.Y. Shenouda, H.K. Liu, *J. Alloy. Compd.*, 477 (2009) 498.
31. H. Gao, Z. Hu, K. Zhang, F. Cheng, J. Chen, *Chem. Commun.*, 49 (2013) 3040.
32. S. Karthickprabhu, G. Hirankumar, A. Maheswaran, R.S.D. Bella, C. Sanjeeviraja, *Ionics*, 21 (2015) 345.
33. X. Wu, G.-L. Xu, G. Zhong, Z. Gong, M.J. McDonald, S. Zheng, R. Fu, Z. Chen, K. Amine, Y. Yang, *ACS Appl. Mater. Interfaces*, 8 (2016) 22227.
34. P. Dou, Z. Cao, C. Wang, J. Zheng, X. Xu, *Chem. Eng. J.*, 320 (2017) 405.
35. E.Z. Xu, H.M. Liu, K. Park, Z. Li, Y. Losovyj, M. Starr, M. Werbianskyj, H.A. Fertig, S.X. Zhang, *Nanoscale*, 9 (2017) 3576.
36. S.H. Mousavi-Zadeh, M.B. Rahmani, *Surf. Rev. Lett.*, 25 (2018) 1850046.
37. B.-g. Zhai, Q.-l. Ma, L. Yang, Y.M. Huang, *J. Nanomater.*, (2018) 7418508.
38. A.C.W.P. James, J.B. Goodenough, *J. Solid State Chem.*, 76 (1988) 87.
39. J. Zhao, Z. Wang, H. Guo, X. Li, Z. He, T. Li, *Ceram. Int.*, 41 (2015) 11396.
40. T. Kim, H. Kim, J.-M. Han, J. Kim, *Electrochim. Acta*, 253 (2017) 190.
41. S. Wang, Y. Zhao, C. Li, X. Zhang, Y. Chen, *J. Alloy. Compd.*, 695 (2017) 1285.
42. W. Wang, J. Zhang, Z. Jia, C. Dai, Y. Hu, J. Zhou, Q. Xiao, *Phys. Chem. Chem. Phys.*, 16 (2014) 13858.
43. X. Tu, Y. Zhou, Y. Song, *Appl. Surf. Sci.*, 400 (2017) 329.
44. W. Yiming, G. Giuli, A. Moretti, F. Nobili, K.T. Fehr, E. Paris, R. Marassi, *Mater. Chem. Phys.*,

155 (2015) 191.
45. H. Yuan, X. Wang, Q. Wu, H. Shu, X. Yang, *J. Alloy. Compd.*, 675 (2016) 187.
46. I.D. Johnson, E. Blagovidova, P.A. Dingwall, D.J.L. Brett, P.R. Shearing, J.A. Darr, *J. Power Sources*, 326 (2016) 476.
47. V.M. Mohan, W. Chen, K. Murakami, *Mater. Res. Bull.*, 48 (2013) 603.
48. X.-L. Wu, L.-Y. Jiang, F.-F. Cao, Y.-G. Guo, L.-J. Wan, *Adv. Mater.*, 21 (2009) 2710.
49. S. Kumakura, Y. Shirao, K. Kubota, S. Komaba, *Phys. Chem. Chem. Phys.*, 18 (2016) 28556.
50. J. Ma, Y. Gao, Z. Wang, L. Chen, *J. Power Sources*, 258 (2014) 314.
51. S. Yu, C. Peng, Z. Li, L. Zhang, Q. Xiao, G. Lei, Y. Ding, *Arab. J. Sci. Eng.*, 42 (2017) 4291.
52. J. Shi, L. Liu, S. Kang, X. Chen, B. Shi, *Can. J. Chem.*, 98 (2020) 106